Evolution of active arching in granular materials: Insights from load, displacement, strain, and particle flow

Yu Zhao [a,b,c], Quanmei Gong [a,b,c,*], Yaojie Wu [a,b,c], Jorge G. Zornberg [d], Zhiyao Tian [a,b,c], Xiao Zhang [a,b,c]

[a] Key Laboratory of Road and Traffic Engineering of the Ministry of Education, Tongji University, Shanghai 201804, China
[b] Shanghai Key Laboratory of Rail Infrastructure Durability and System Safety, Tongji University, Shanghai 201804, China
[c] College of Transportation Engineering, Tongji University, Shanghai 201804, China
[d] Department of Civil, Architectural and Environmental Engineering, The University of Texas at Austin, TX 78712-0273, USA

ARTICLE INFO

ABSTRACT

The progressive failure of active soil arching in a quasi-static particle flow was investigated to elucidate the deformation behavior and load evolution mechanism. A transparent trapdoor test apparatus and self-developed particle image velocimetry system were used to capture the soil mass displacement field. Disturbed region and active region were introduced to characterize the displacement patterns evolution for both shallow and deep conditions. Meanwhile, the evolution of the surface settlement, horizontal displacement, and volumetric change of backfill as the trapdoor receding were quantified. The shear band propagation was interpreted considering the dilatancy behavior. In addition, the vorticity reveals local rotation characteristics in the shear region. Afterwards, i) the evolution mechanism of arching was speculated from macro-and microscopic perspectives. ii) The critical displacement for mobilizing the minimum load was discussed. These results can provide a profound understanding for mathematical modelling that is expected to illustrate the progressive development of active arching with displacement.

1. Introduction

The arching effect is a pervasive phenomenon observed in granular materials. It is defined as the load transfer and stress redistribution induced by relative displacement between the soil mass and adjacent underground inclusion [1]. This effect plays a pivotal role in load estimation and deformation control in the design of tunnels, pile-supported embankments, underground conduits, pipelines, plate anchors, and other buried structures [2–7]. Since the pioneer trapdoor tests were conducted by Terzaghi [1] to investigate the arching effect, numerous extensions of this study have been performed in physical laboratory experiments [3,8–11] and more recently using scaled centrifuge modelling [12–16] as well as numerical simulation [9,17–20].

In early studies of the soil arching effect, based on the observed failure mode (e.g., potential vertical, triangular, or parabola shear planes for two-dimensional (2D) conditions; hemispherical shape for three-dimensional conditions), some closed-form solutions for load evaluation on the buried structures were developed using limit equilibrium

methods [1–3,8,21–23]. The limit equilibrium arching models assume that the soil above the underground inclusion or trapdoor is in a yielding (i.e., ultimate) state [24]. Later, Papamichos et al. [25] and Iglesia et al. [16] proposed new cone-shaped and parabolic failure mechanisms, respectively, to describe the behavior of backfill layer with small trapdoor displacement, giving an improved load estimation on small displacement conditions. However, all of the aforementioned models, which assume a fixed geometric shape to simulate "soil arching" to describe only one point on the arching load-displacement curve, focus on load evaluation and a specific state behavior, commonly ignoring the deformation characteristics. King et al. [26] highlighted the need for coupled arching load-displacement or stress-deformation models to describe the serviceability behavior accurately for practical applications. Han et al. [24] emphasized the progressive development of 2D soil arching with relative displacement. If the displacement of the soil is limited, soil arching is referred to as *partially mobilized soil arching*. Therefore, it should be emphasized that the mobilized displacement, relative load, and corresponding deformation behavior are highly important for certain geotechnical applications (e.g., deformation and corresponding load transfer quantity on pile-supported embankments [27]; settlement and corresponding supporting pressure when tunneling [7]).

Recently, several studies have also focused on the evolution of arching effect with increasing mobilized displacement from different aspects. i) Regarding deformation patterns and failure mechanisms,

Chevalier et al. [9] conducted a series of trapdoor tests and described the load-transfer processes in three phases: phase (a): the maximum transfer phase, phase (b): the transitional phase, and phase (c): the critical phase. A triangular expansion zone was observed in phase (b), whereas phase (c) showed a vertical column-like mechanism. Iglesia et al. [16] carried out a series of centrifuge tests and also identified three development stages. Rui et al. [18,28] used 2D multi-trapdoor test setup, a series of model tests with sand fills were conducted to study the soil-arching type and its development. Jacobsz [29] used particle image velocity (PIV) technique to capture shear bands progressively propagating through the granular materials in the transitional phase. Lai et al. [19] performed discrete element method (DEM) simulations to develop a reasonable classification system for soil arching structures with emphasis on the embankment deformation behavior. ii) Regarding the mobilization mechanisms of "soil arching", from a microscopic perspective, load transfers are the results of particle rearrangements and reorientation of force chain according to the arch patterns above the trapdoor [9]. The contact force rotation induced by the relative displacement causes changes in the load-transfer path, altering the stress distribution [30]. iii) Regarding the load–displacement response, most researchers have observed that an initial load decreases rapidly to a minimum value and then recovers up to a constant load [9,16,24]. In summary, all of these experimental and numerical results provide basic information on arching evolution. However, most of the previous studies have been limited to one aspect. For instance, the failure mechanism of the soil mass and the load–displacement response of the trapdoor have been studied independently. This separation is not conducive to elucidating the relationship between load transfer and deformation. More importantly, there seems no recognized and reasonable interpretation for load–displacement response curves. When is the arching mobilized (i.e., the corresponding mobilized displacement) and how does it evolves? Therefore, it is necessary to understand the evolution of soil arching with trapdoor displacement from different perspectives and to develop a comprehensive framework, to facilitate the establishment of a more accurate and evolutionary mathematical model that couples the arching load with the mobilized displacement or arching deformations.

As continuous deformation and strain distributions in trapdoor tests can provide considerable insight into the evolution of arching, but due to the difficulty of measuring such strains with conventional methods, e.g., discrete markers to track the soil movement [12,14], they are rarely presented in the literature. Recently, using Digital Image Correlation (DIC) technique, Khatami et al. [6,10,31] measured the displacements and strains within a soil cross-section to evaluate the soil deformation conditions that lead to active or passive arching. However, more attention was paid to the test technique and the effect of a surcharge on arching in rubber-sand mixtures than to the evolution of soil arching. The ability to measure the displacement and strain development in laboratory tests in conjunction with load evolution will enhance understanding of the evolution of the arching phenomenon mobilized by relative displacement, serving as an impetus for further physical experimentation.

This study aims at making a deep understanding on the evolution of active arching in granular materials from different perspectives, focusing on the deformation behavior, load evolution, and progressive failure mechanisms. Further, the intrinsic relations among these behaviors were assessed. A trapdoor apparatus was installed with a series of sensors and high-speed imaging equipment was utilized. With the help of the self-developed PIV system, the evolution of the soil particle displacement was obtained. The load evolution was evaluated in conjunction with deformation behavior during the arching process.

2. Laboratory trapdoor investigation

2.1. Testing apparatus

Fig. 1 shows the model test equipment, which consists of three parts: the model container, trapdoor device, and measurement system. i) The model container for the soil is made of smooth plexiglass plates with high transparency to minimize the boundary friction with the backfill and to guarantee optimal imaging during testing. The internal dimensions of the container are 700 mm in length, 300 mm in width, and 700 mm in height. ii) To achieve a plane strain condition, the trapdoor device is installed at the bottom and center of the soil box, with a width (B) of 150 mm and a length (L) of 300 mm [Fig. 1 (b)]. A variable frequency motor is placed on the bottom of the model container, which is connected to a load sensor that is mounted to the base of the trapdoor. The applied load on the trapdoor and corresponding displacement can be accurately acquired when it rises or falls. iii) The measurement system, in addition to the sensors mentioned above, also includes surface displacement measurement sensors, particle image velocity measurement system, and data acquisition equipment. The data acquisition frequency was 2 Hz in this study, and all the collected data were displayed on the computer screen in real time, as shown in Fig. 1 (a). The following section introduces the PIV system in detail.

2.2. Self-developed PIV system and analysis procedure

PIV technique works by continuously capturing high-resolution digital images in the process of material deformation in geotechnical laboratory tests. Then, each image is divided into a finite grid composed of subset patches, which are identified by their own texture features together with light and shadow features when illuminated [31–33]. The displacement offset of each subset patch is determined by using image matching technology between two images [34]. As a plane-strain
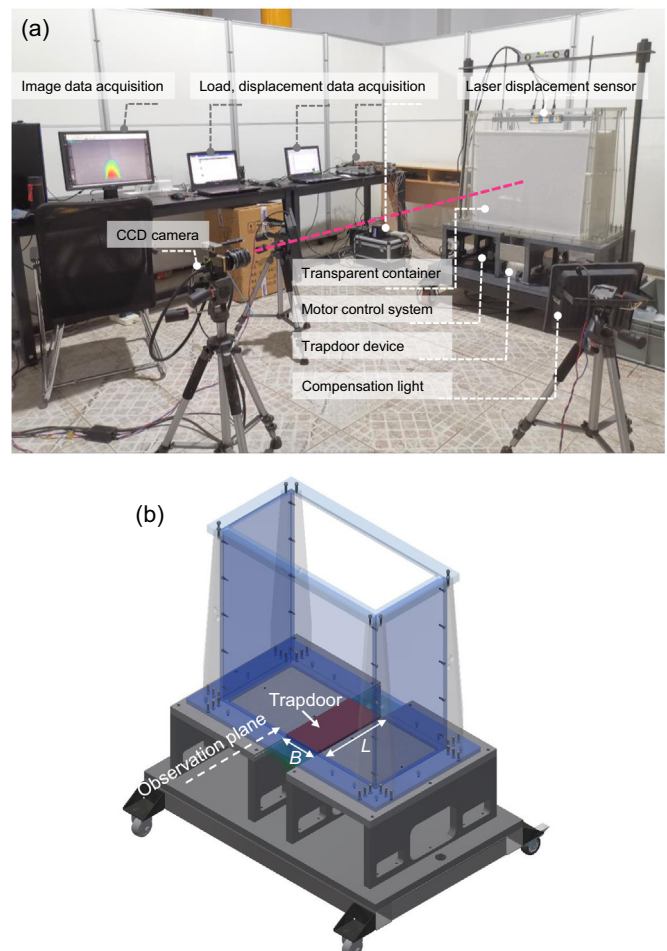

Fig. 1. (a) Model test setup. (b) Scheme diagram of the trapdoor apparatus.

problem in this study, a 2D PIV system was developed to track the movement in the soil body. The observation and analysis system included a charge-coupled device (CCD) camera, an image acquisition board, a computer, the PIV analysis software, and a compensation light source. A research-grade CCD camera with a resolution of 2456×2056 pixels (the pixel size is 3.45 um) was used. State-of-the-art microvec3 software was used as camera controlling and image processing software to determine the incremental and total displacements of the soil particles.

To convert the PIV displacement results into actual particle displacements, a scale plate was set on the bottom of the model container, as shown in Fig. 2. The calibration ratio C_s, which is defined as the actual displacement divided by corresponding displacement obtained from the images was used. In this study, C_s was 0.265 mm/pixel for typical tests. Fig. 2 shows some of the images captured or post-processed during the test. Fig. 2(a) shows distinguishable spots when illuminated by the light. Fig. 2(b) presents a typical monochrome image, which exhibits notable texture features, making it conducive to PIV analysis. Fig. 2(c) shows a typical grid after calibration, where the size of a subset patch is 4.13 mm × 4.13 mm.

2.3. Granular properties

The Particle Size Distribution (PSD) of the fused quartz sand shows that 95% of the particles were in the range of 0.5–1 mm. According to the Unified Soil Classification System (USCS), this sand is classified as poorly graded sand (SP). More properties of this sand are summarized in the Table 1. The friction angle, as determined by axisymmetric triaxial tests, is higher than that of natural sand because of the angular particle of fused quartz sand but is close to the values for the same material reported in other studies [35].

2.4. Experimental procedure

The sand bed was prepared in several layers by pouring sand particles into the testing container via air pluviation method. After that, the CCD camera was placed at the same height and horizontal position as the center of the specimen. Meanwhile, the axis of the CCD camera was parallel to the longitudinal axis of the trapdoor to ensure that the entire area required for displacement analysis would be located in the image frame and that the image displacement was proportional to the actual displacement. Four tests were performed, including four embedment ratios of i (i = H/B, where H is the buried depth of trapdoor),
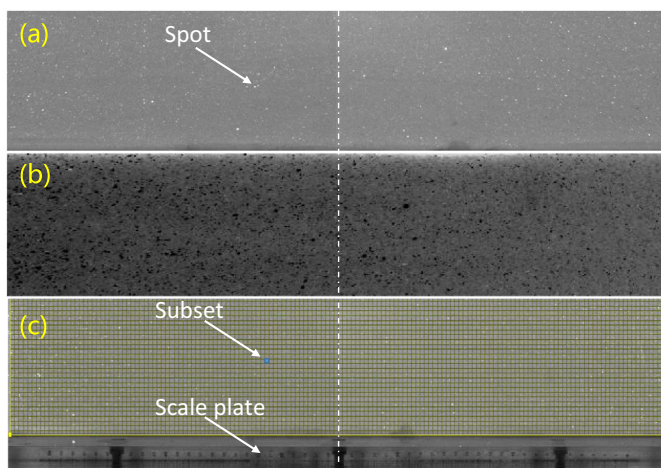

Fig. 2. Images captured or post-processed through PIV. (a) Original image depicting a spot pattern in the soil mass. (b) Typical monochrome image. (c) Typical area of computational grid and corresponding subset after calibration for PIV analysis.

Table 1
Physical and mechanical properties of quartz sand in this study.

Characteristics	Value
Maximum dry density ρ_{max} (g/cm^3)	1.286
Minimum dry density ρ_{min} (g/cm^3)	1.030
Specific gravity G_s (unitless)	2.186
Mean particle size D_{50} (mm)	0.7
Coeffcient of curvature C_c (unitless)	0.99
Coeffcient of uniformity C_u (unitless)	1.42
Peak friction angle φ_p (°)	45.6
Moisture content ω (%)	0
Relative density D_r (%)	60
Backfill gravity density γ (kN/m^3)	11.46

i.e., 1, 2, 3 and 4. All the tests were initiated by moving the trapdoor downward at a constant speed of 2.0 mm/min until the displacement reached 30.0 mm, which took 900 s. The camera takes pictures at 2 frames/s, which is consistent with the acquisition frequencies of other sensors. The response of backfill was considered to quasi-static granular flow as a relatively low velocity [9].

3. Results: four perspectives

In this section, the evolution of arching effect will be presented from four different perspectives, corresponding to the response of trapdoor (Section 3.1) and backfill (Sections 3.2–3.4). Firstly, according to the load evolution characteristics, the evolution of arching effect can been divided into different stages; further, the kinematic characteristics of backfill in different stages were deduced from the PIV analysis. In particular, it will present the distributions of the displacement, surface settlement, volumetric change behavior, strain, time-average velocity, and vorticity in typical stages in detail, providing more comprehensive perspectives to elaborate the load evolution and deformation behavior of arching.

3.1. Load evolution

The load–displacement response provides the most intuitive insight into the load transfer on trapdoor. Fig. 3 presents the load–displacement responses of trapdoor. The trapdoor displacement (δ) was normalized by the width of the trapdoor (B), whereas the load was normalized by the original self-weight value (γBLH). As studied by previous researches [3,16], an initial sharp drop in load was observed, followed by an increase towards to an eventual constant load. This load response of the soil-arching with the relative displacement can be divided into four stages (as shown in Fig. 4). (i) Stage a - initial soil arching: Once the trapdoor is lowered, it can be observed that the load on the trapdoor (ρ) begins to drop sharply and approximately linearly decreases with the displacement (Δ). (ii) Stage b - maximum soil arching: At this stage, the load slowly and linearly decreases to the minimum load point (Δ_{min}, ρ_{min}), corresponding to the maximum soil arching where the greatest load is carried by the arch. (iii) Stage c- load recovery: After the maximum soil arching, the load increases gradually with displacement and recovers up to an ultimate load. This transition is approximately linear. (iv) Stage d - ultimate state: The load recovery stage stops at the critical point (Δ_{ult}, ρ_{ult}) when soil arching reaches the ultimate state. The further retraction of the trapdoor will not lead to a greater load. This developed load evolution was so-called Ground Reaction Curve (GRC) as mentioned by Iglesia et al. [5]. After that, Han et al. [24] suggested a simplified representation of the GRC method and termed their model the "simplified GRC." In the simplified GRC, the arching load development is simplified and described as three linear lines, as shown in Fig. 4. Hence, two points, (Δ_{min}, ρ_{min}) and (Δ_{ult}, ρ_{ult}), are the key parameters to determine the simplified GRC. Han et al. [24] suggested ultimate load (ρ_{ult}) and minimum load (ρ_{min}) can be
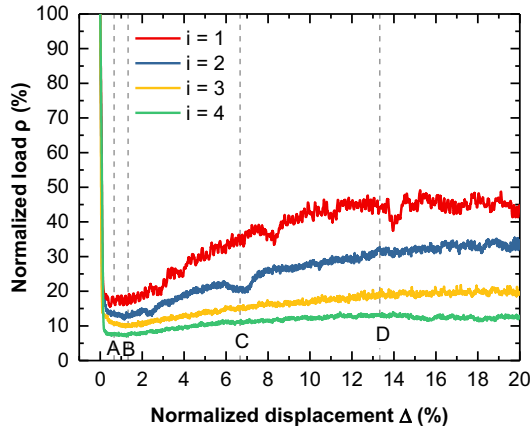
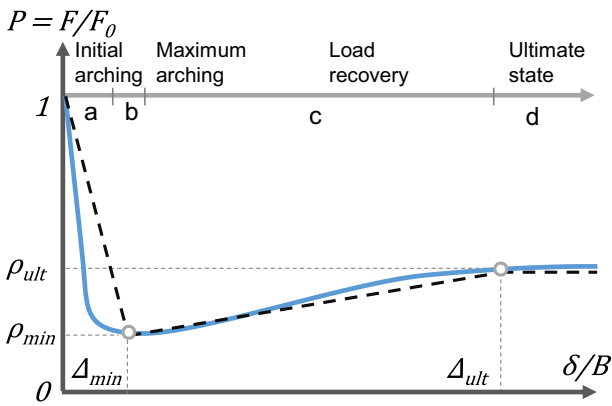**Fig. 3.** Load–displacement curves for active arching.

Fig. 4. Normalized load versus normalized displacement to describe the four successive phases of the active trapdoor problem (modified from Iglesia et al. [5] and Han et al. [24]).

calculated using Terzaghi's method [1] by Eq. (1) and Iglesia's method [16] by Eq. (2), respectively.

$$\rho_{ult} = \frac{B}{2KH\tan\varphi}\left(1 - e^{-2K\tan\varphi \cdot \frac{H}{B}}\right) \tag{1}$$

$$\rho_{min} = \frac{B}{H}\left(\frac{K_E}{2\cot\varphi + \frac{B}{H}K_E} + \frac{\cot\varphi}{6}\right) \tag{2}$$

where B is the width of the trapdoor, φ is the effective friction angle of soil, H is the height of the backfill, K is the lateral earth-pressure coefficient, and K_E can be expressed as $\cos^2\varphi/(1 + \sin^2\varphi)$ and derived by considering the Mohr circle. The ultimate stage was associated with considerable deformation, making it seem fairly intuitive to accept that the shear strength of the material corresponded to the critical friction (i.e., $\varphi = \varphi_c$ in Eq. (1)). In the minimum load state, however, the very small displacement of the trapdoor means a minor strain level, suggesting that the peak friction angle is more reasonable (i.e., $\varphi = \varphi_p$ in Eq. (2)).

In the load recovery stage, the slope of the GRC shown in Fig. 4 can be defined as the load recovery index λ_{rec}:

$$\lambda_{rec} = \frac{\rho_{ult} - \rho_{min}}{\Delta_{ult} - \Delta_{min}} \tag{3}$$

λ_{rec} represents the ability of the granular material to maintain the load transfers obtained at the end of minimum load stage: high values of λ_{rec} mean that the load transfers decrease rapidly or arching roof

collapse occurs remarkably, whereas low values of λ_{rec} correspond to good load transfer conservation [9]. This increased vertical load on the trapdoor may be contributed by two reasons: i) the reduced angles of friction and dilation resulting from the decreased shear strength and ii) an increasing volume of loose soil mass being carried by the trapdoor as the inclined slip surface evolves into a vertical slip surface. This shape evolution will be discussed in Section 3.2.

According to the values of Δ_{min} and Δ_{ult} suggested by Han et al. [24], a simplified method of evaluating λ_{rec} can be expressed as Eq. (4a). Iglesia et al. [5] also provided an empirical method based on the centrifuge trapdoor experiment using Eq. (4a). Fig. 5 compares the results of these methods with the test results, demonstrating that the simplified method can evaluate λ_{rec} well, whereas the empirical method evaluates it to be larger than test results. This may be due to the fact that some fitting constants obtained by the empirical method are not suitable for this test condition. It should be noted that in the simplified method, the most critical parameter is the friction angle, whereas the ratio of the trapdoor width to the particle size is the key input parameter in the empirical method. In any case, all of the results show that the load recovery index decreases with increasing embedment ratio.

$$\lambda_{rec} = \frac{\rho_{ult} - \rho_{min}}{10\% - 1.5\%} \tag{4a}$$

$$\lambda_{rec} = \left[2.5 + 5.7\log\left(\frac{B}{10D_{50}}\right)\right]e^{-0.65(H/B)} \tag{4b}$$

3.2. Development of displacement

3.2.1. Total displacement (S_T)

To some extent, the displacement can present some features of arching evolution and can be used to identify the characteristics of the soil arching structure [18,19]. Table 2 shows the distribution of total displacement (S_T) in different load evolution stages. Typically, the evolution of displacement is quite different between shallow (e.g., $i = 1$) and deep buried conditions (e.g., $i = 2, 3, 4$) [14]. For the shallow buried condition, the captured displacement region, herein called the "disturbed region", is approximately trapezoidal in the initial stage and evolves into a rectangular region. While, it forms an inverted trapezoidal region in the ultimate state. For the deep buried condition, a roughly triangular region is observed in each test at a small displacement (e.g., $\delta = 1$ mm). This phenomenon is consistent with the findings of Rui et al. [18]. However, a parabolic shape of the disturbed region, as mentioned by Iglesia et al. [16], is not observed. In the initial arching stage, the height of disturbed region increases with increasing embedment ratio with the same trapdoor displacement (e.g., $\delta = 1$ mm). For
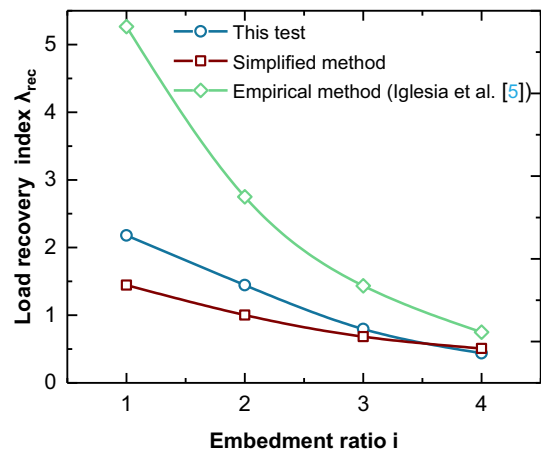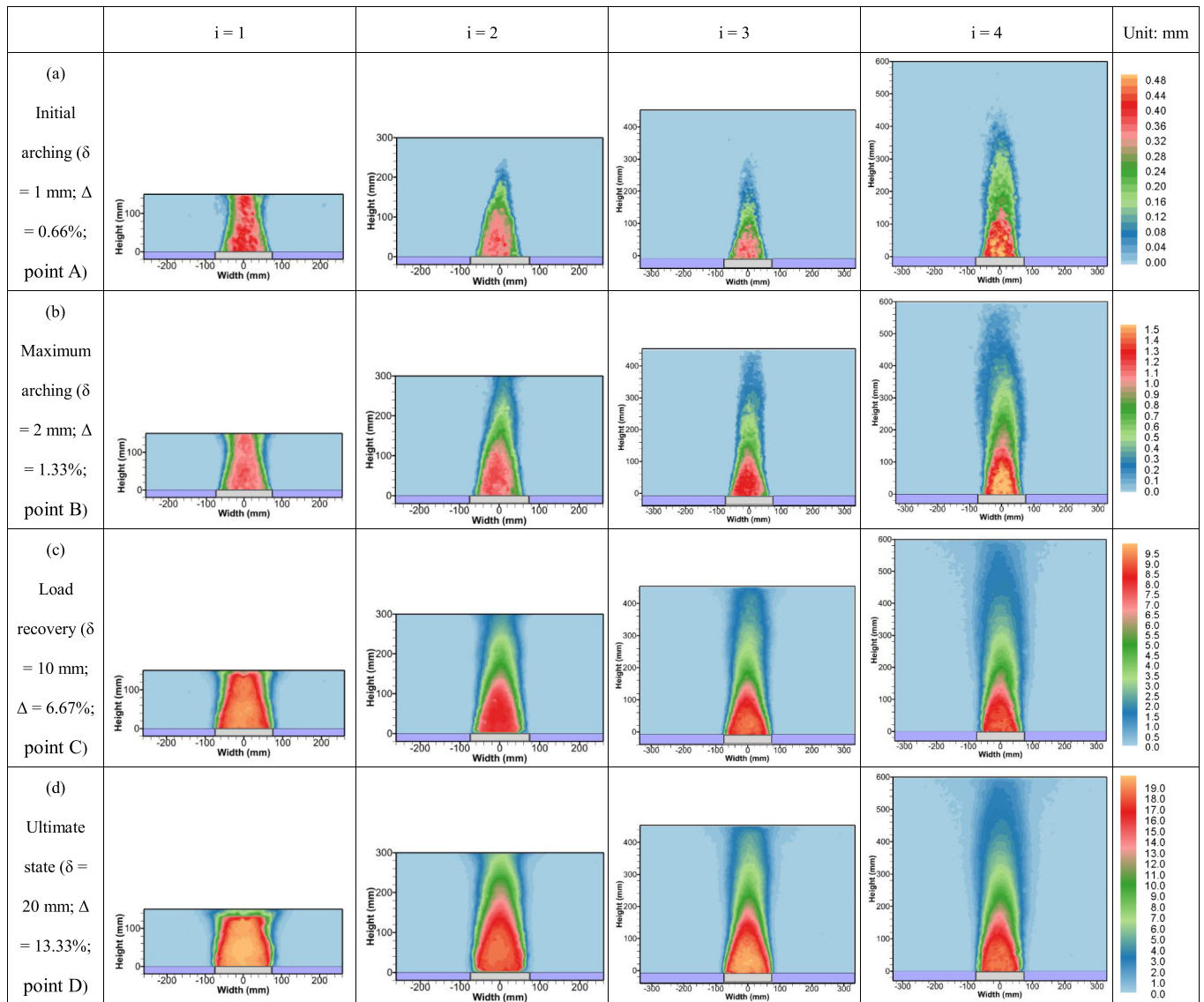

Fig. 5. Load recovery index versus embedment ratio.

Table 2
Displacement fields at different embedment ratios and in different load evolution stages.

Note: Points A, B, C, and D have been marked in Fig. 3. At the stage of load recovery and ultimate state in embedment ratio of 1, the PIV data on the surface may be incorrect because of the conspicuous settlement trough.

example, when the embedment ratio is 2, 3, and 4, the height of the disturbed region is approximately 1.7B (250 mm), 2.1B (320 mm), and 3B (450 mm) respectively, which means that the base angle of the triangle increases with increasing embedment ratio, i.e., the boundary of the disturbed region becomes steeper. As the trapdoor recedes further (e.g., δ = 2 mm), the region gradually extends upwards towards soil surface with increasing base angle of the triangle. This time, the region corresponding to the shallower buried condition reaches the surface first, although the boundary of the disturbed region is flatter in the previous stage. After evolution to the surface, the region takes on the shape of a trapezoid instead of a triangle (e.g., in the load recovery stage). It further evolves into a rectangular region or even an inverted trapezoidal region (e.g., in the ultimate stage). The disturbed region can give an intuitive and visual evolution on particle movement, providing an

opportunity and more information for understanding the evolution mechanism of soil arching.

In terms of the evolution of the disturbed region, perhaps the most difference between the deep and shallow conditions is that this region will not experience evolution from the local region above the trapdoor to the surface for shallow buried conditions. Once the trapdoor recedes, a significant "active region" originates from the trapdoor bottom and extends to the surface, indicating that the maximum surface settlement is close to the displacement of the trapdoor. As the downward of trapdoor, the active region evolves from an approximately trapezoidal zone into a rectangular zone. For deep buried conditions, however, this active region is limited to a parabola-shaped zone rather than developing to the surface (red area in Table 2), where the displacement is considerably large and approximately same as the displacement of

the trapdoor. Especially, this active region also tends to extend upwards with the trapdoor displacement.

To better illustrate the evolution of the active region, the vertical displacement of soil at different heights above the centerline of the trapdoor were extracted at a typical embedment ratio of 3 (shown in Fig. 6). Vertical displacement is negligible in the initial stage. When the curve reaches the 1:1 line, it means that the corresponding position moves down with the trapdoor as a whole and achieves a "fully active region". In the maximum arching stage, the soil at the height of 50 mm enters into the fully active region (i.e., point A in Fig. 6). As the trapdoor is displaced further downward, the soil at the heights of 100 mm, 150 mm, and 250 mm enters into the fully active region successively (i.e., points B, C, and D in Fig. 6).The results about the evolution of the disturbed and active regions can be better illustrated in Fig. 7, corresponding to deep and shallow conditions, respectively.

3.2.2. Horizontal displacement (S_H)

Importantly, this deformation behavior can provide a unique perspective for interpreting the evolution of soil arching effect. Fig. 8 showed the typical distribution of S_H in the soil body for different embedment ratio. Overall, S_H is quite small comparing with the displacement of the trapdoor (e.g., $\delta = 20$ mm). Meanwhile, there is almost no S_H in an approximately parabolic region above the trapdoor, which indicates that this area moves vertically with the trapdoor as a whole. This is also consistent with the concept of active region proposed in previous section. Above the parabolic region, the vertical downward movement of the trapdoor causes the particles in the upper and shallow layers to move horizontally from the original position to the position of the symmetry axis. Fig. 8 also shows that significant differences can be observed between shallow and deep buried conditions. For instance, the maximum value of S_H occurs in shallow layers near the surface for the shallow condition (e.g., $i = 1$), whereas it appears in deep layers for the deep condition (e.g., $i = 3$).

3.2.3. Surface settlement (S_S)

The surface subsidence distribution was captured by tracking the movement of subset patches near the surface using PIV. The data from PIV correlated well with the laser displacement sensor measurements. Costa et al. [14] suggested that Ss can be expressed as Gaussian curves (shown in Fig. 9). Fig. 10 compares the settlement troughs to Gaussian curves. The settlement trough has the shape of a Gaussian curve initially but deviates from this shape as the trapdoor moves deeper. This deviation occurs because the maximum surface settlement ($S_{S,max}$) deviates from the axis of the trapdoor. In the Gaussian curve, one of the most critical parameters is $S_{S,max}$. Fig. 11 shows the development of this value for different embedment ratios. $S_{S,max}$ is approximately equal to δ for $i = 1$,
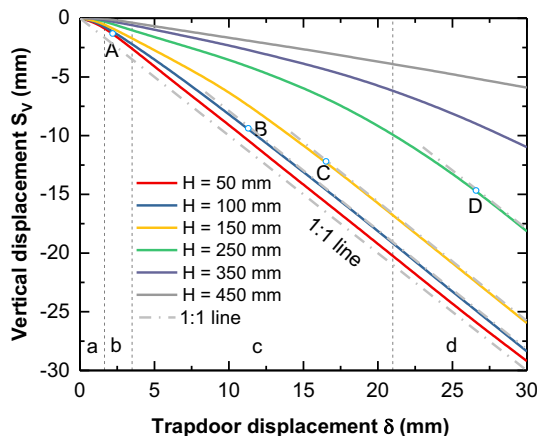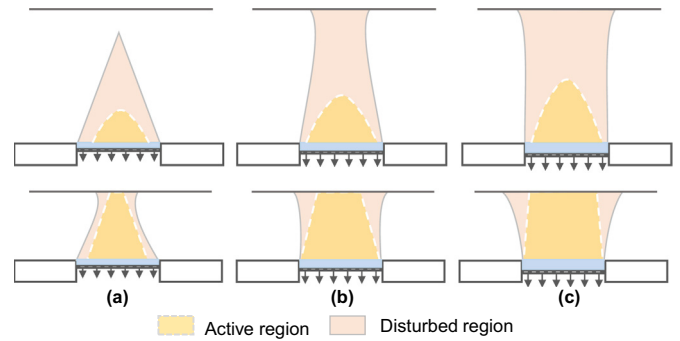
Fig. 7. Evolution of displacement patterns for deep and shallow buried conditions. (a) Initial and maximum arching stage. (b) Load recovery stage. (c) Ultimate stage.

significantly smaller than δ for $i = 2$, and barely visible for $i = 3$ and 4. All of these curves present two stages characteristics; that is, the surface settlement rate is obviously lower than the trapdoor displacement rate in the initial and maximum arching stages, whereas in the load recovery and ultimate stages, the settlement rate increases obviously. Combining GRC curve, this feature can be better illustrated in Fig. 12. At the initial stage, the surface settlement can hardly be observed. Basically, the displacement corresponding to break point of GRC equal to that of settlement curve. The x-coordinate corresponding to the break point can be regarded as the critical displacement (Δ_{cri}) at which the disturbed region reaches the surface and begins to develop significantly. In particular, Δ_{cri} is roughly equal to Δ_{min}.

3.2.4. Volumetric change (ΔV)

As discussed previously, there is almost no surface settlement at the initial stage, and the surface settlement gradually increases as the trapdoor moves down, indicating that the backfill material has obvious volume dilation. This volume change behavior can be better illustrated in Fig. 9. Here, the ground loss (V_L), surface settlement volume (V_S), and the volumetric change of disturbed domain (ΔV) were calculated using Eq. (5). As a plane strain problem, the unit width was taken for analysis, and S_S was obtained from the PIV data. As expected in Fig. 13, V_S is much smaller than V_L for dilation of backfill.

$$V_L = B \times \delta \tag{5a}$$

$$V_S = \int_{-\infty}^{+\infty} S_S(x)dx \tag{5b}$$

$$\Delta V = V_L - V_S \tag{5c}$$

Similar to the definition of volume strain, the volumetric change ratio λ is defined as ΔV divided by the volume of the disturbed region (V) in Eq. (6a), which describes the degree of looseness of the backfill during the test. Meanwhile, the volumetric change rate μ is defined as ΔV divided by V_L in Eq. (6b), which is related to the secant slope of the volumetric expansion curve in Fig. 13 and can describe the degree of dilatation occurring in the soil body during the test. Fig. 14 presents λ and μ at embedment ratio of 3. Initially, μ keeps the maximum value of 1. This is because there is no surface settlement, and ΔV equal to V_L, indicating a significant dilation. Then μ decreases rapidly in the initial and maximum arching stages. The maximum shear stress was mobilized in the soil body in a relatively small displacement, achieving the maximum active arching. As the trapdoor receded further, μ slowly decreased with continuous dilation but remain a lower rate, corresponding to a load recovery stage. However, λ steadily increases during the whole process. Because the surface settlement is significantly smaller than the displacement of trapdoor, volumetric expansion develop continuously in the soil (Fig. 13). According to ΔV, the compactness in the disturbed region of backfill material can also be obtained. In this

Fig. 6. Vertical displacement at different heights above the trapdoor center ($i = 3$).

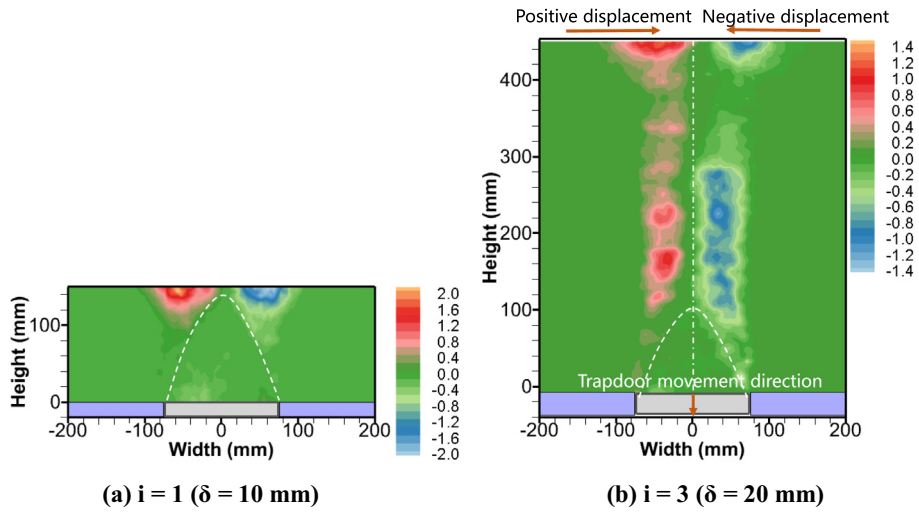**(a) i = 1 (δ = 10 mm)**   **(b) i = 3 (δ = 20 mm)**

Fig. 8. Distribution of horizontal displacement in the soil body. (a) Shallow. (b) Deep.
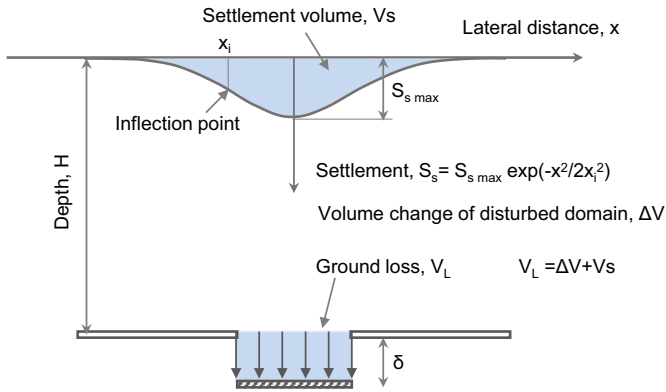

Fig. 9. Schematic diagram of ground loss and surface settlement characteristics of active trapdoor.
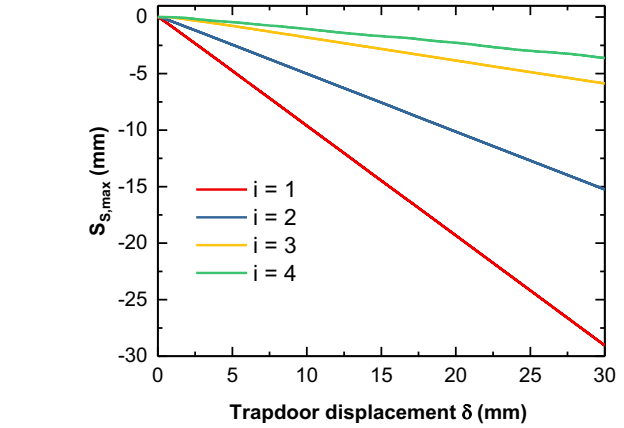

Fig. 11. Development of maximum surface settlement with trapdoor displacement at different embedment ratios (data from laser displacement sensor).

experiment, the initial relative density Dr_0 was 60%. At the end of the experiment, the average relative density in the disturbed region reached the minimum value of 33.6%, indicating that a relatively loose state was achieved.

$$\lambda = \frac{\Delta V}{V} = \frac{B \cdot \delta - \int_{-\infty}^{+\infty} S_S(x) dx}{BH} \tag{6a}$$

$$\mu = \frac{\Delta V}{V_L} = \frac{1}{B} \cdot \frac{\Delta V - 0}{\delta - 0} = \frac{1}{B} \cdot k(\delta) \tag{6b}$$
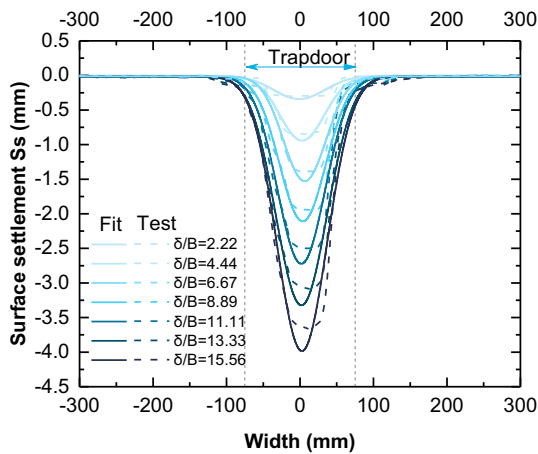

Fig. 10. Distribution and development of surface settlement with trapdoor displacement (i = 3; unit of δ/B: %).
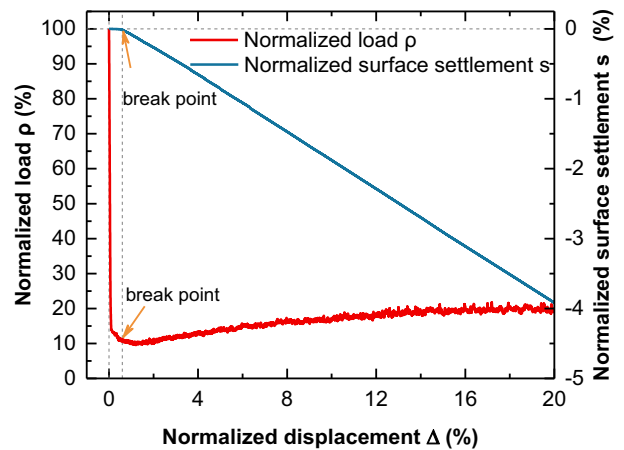

Fig. 12. Load–displacement curves and corresponding maximum surface displacements at embedment ratio of 3.
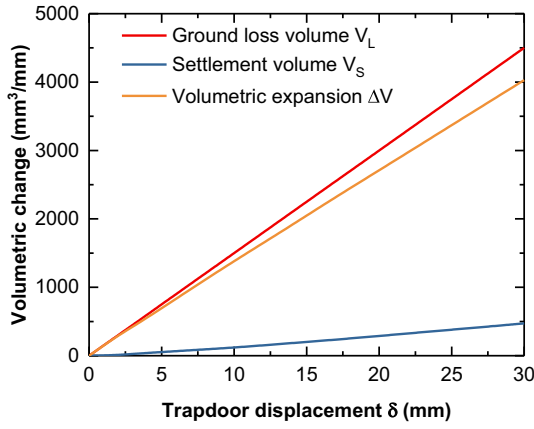
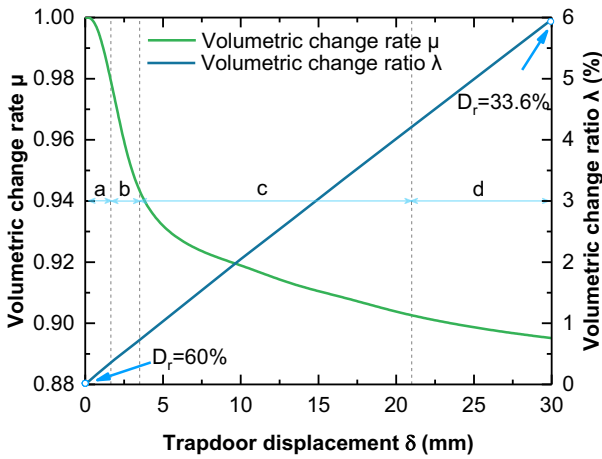**Fig. 13.** Volumetric change with the trapdoor displacement (i = 3).

Fig. 14. The volumetric change ratio λ and the volumetric change rate μ versus the trapdoor displacement (i = 3).

3.3. Development of strain

Displacement data from microvec3 were further processed to obtain the strain with the help of TECPLOT software. Consequently, more in formation about the mesoscopic mechanism of soil deformation was visualized. The Green-Lagrange strains were calculated from the displacement field as Eq. (7):

$$
\begin{aligned}
\varepsilon_{xx} &= \frac{\partial u}{\partial x} + \frac{1}{2}\left[\left(\frac{\partial u}{\partial x}\right)^2 + \left(\frac{\partial v}{\partial x}\right)^2\right] \\
\varepsilon_{yy} &= \frac{\partial v}{\partial y} + \frac{1}{2}\left[\left(\frac{\partial u}{\partial y}\right)^2 + \left(\frac{\partial v}{\partial y}\right)^2\right] \\
\gamma_{xy} &= \frac{\partial u}{\partial y} + \frac{\partial v}{\partial x} + \left(\frac{\partial u}{\partial x}\frac{\partial u}{\partial y} + \frac{\partial v}{\partial x}\frac{\partial v}{\partial y}\right) \\
\gamma_{max} &= \sqrt{\left(\varepsilon_{xx} - \varepsilon_{yy}\right)^2 + \gamma_{xy}^2}
\end{aligned}
\tag{7}
$$

where u is the horizontal displacement, v is the vertical displacement, ε_{xx} is the horizontal strain, ε_{yy} is the vertical strain, γ_{xy} is the shear strain, and γ_{max} is the maximum shear strain.

3.3.1. Propagation of shear band

Table 3 shows the distributions of the incremental maximum shear strain (γ_{max}^i) at typical stages corresponding to the load evolution. γ_{max}^i represents the change between the current image and previous
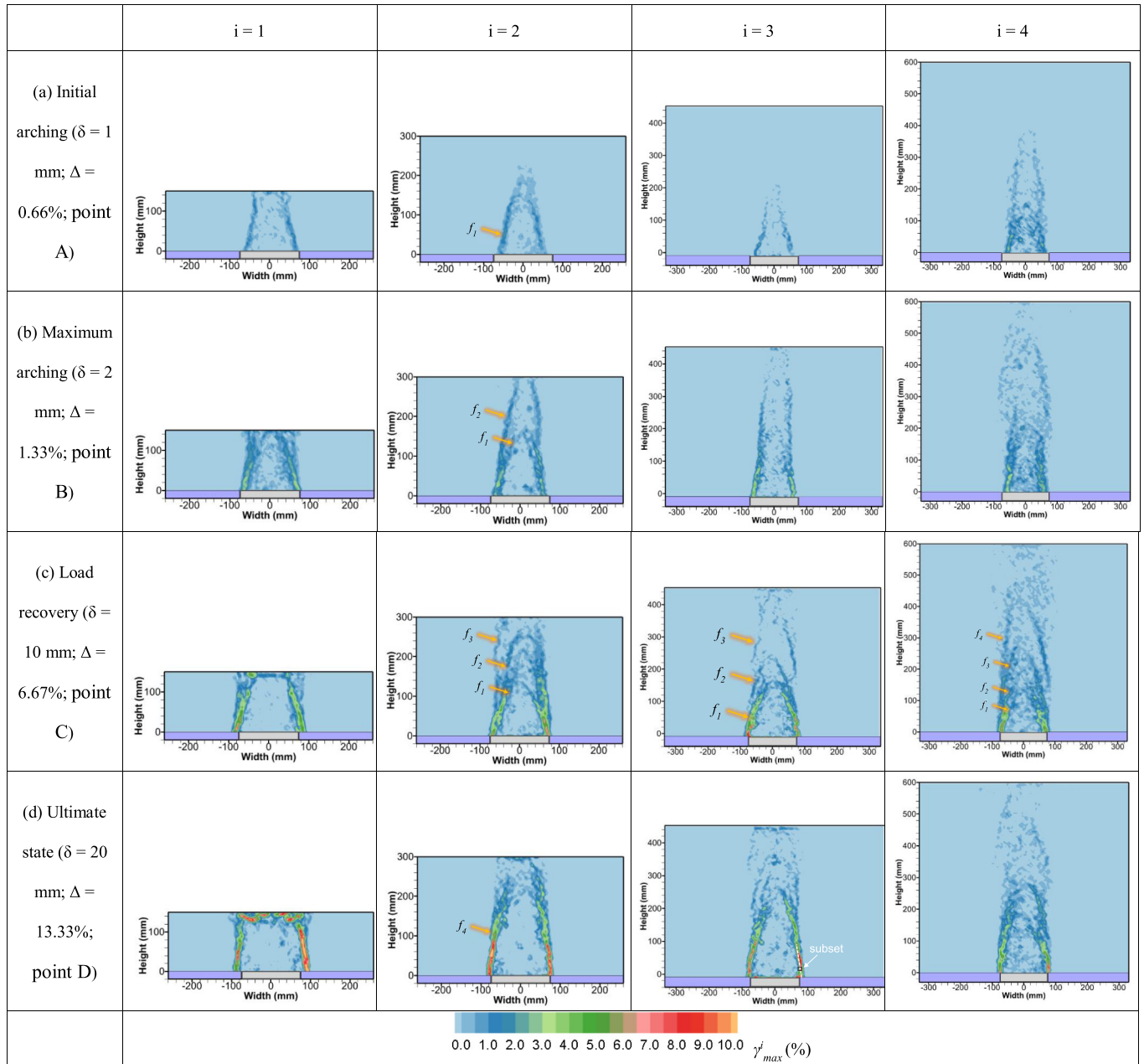
image with a trapdoor displacement step of 1 mm. This deformation behavior in these typical stages illustrate the development of arching and elucidate the progressive failure mechanism. Overall, from the γ_{max}^i, it is evident that two prominent shear bands appear on the inner side of the trapdoor edge and extend to the surface or converge at the center of the soil in the initial arching stage, forming an initial trapezoidal or triangular shape, depending on the buried depth. As the trapdoor receded further, the root of the shear band gradually moves to the outside of the trapdoor edge, with a decreasing inclination angle that measured between the shear band and vertical plane. Similarly as the development of displacement, two significantly different development patterns can be observed, namely, the failure mechanisms on shallow (i.e., $i = 1$) and deep (i.e., $i = 2, 3,$ and 4) conditions. There seems to be a critical embedment ratio (i_{cri}) between 1 and 2, where the primary shear band (labelled f_1) at small displacement (i.e., $\delta = 1$ mm) just extends to the surface and converges at the center of the surface.

For the shallow conditions, in the initial and maximum arching stages, the shear bands cannot meet at the center of the soil body or surface; thus, a trapezoidal region is formed. Subsequently, the slopes of the shear bands become steeper in the load recovery stage, until the ultimate state forms an approximately vertical shear band. For the deep conditions, the development of shear band seems more complicated, as multiple shear bands can be observed successively in Table 3. Two primary shear bands (labelled f_1) form and take on the shape of a triangle from the two inner edges of the trapdoor initially. Then, the tops of the primary shear bands unfurl and extend upwards, followed by branches of secondary shear bands (labelled f_2) radiating inward on the basis of the primary shear bands with increasing trapdoor displacement. New shear bands (labelled f_3 and f_4) continue forming above them and expand upwards towards the soil surface with generally decreasing intensity of shear strain. All of these following shear band pairs meet at the center of the soil mass, forming an approximate parabola, rather than the initial triangular shape.

To achieve a better understanding the propagation of shear band, the shear strains were extracted along four profiles (at typical embedment ratio of 3), namely, at heights of 0 mm ($y = 0$ mm), 50 mm ($y = 50$ mm), and 100 mm ($y = 100$ mm) above the trapdoor and at the vertical profile located at $x = 50$ mm, parallel to the trapdoor axis. Fig. 15 shows the development of γ_{max} and γ_{xy} with the trapdoor displacement in the horizontal profile at $y = 50$ mm. There are two strain peaks near the inner edge of the trapdoor. However, in the area within these two peaks, the strain is quite small. Meanwhile, with increasing trapdoor displacement, the horizontal position of the peak strain moves far away from the center of the trapdoor and closer to the edge of the trapdoor, which means that the vertical inclination angle of the shear band becomes closer to zero. This is consistent with the evolution characteristics of the shear band shown in Table 3. The development of γ_{max} at $y = 100$ mm presents similar characteristics, and the position of the peak strain at $y = 100$ mm was extracted. The inclination angles of the shear bands of the initial portion (measured from the vertical direction) were calculated by linking the positions of the peak strain at $y = 100$ mm and $y = 0$ mm. Fig. 16 provides the development of the inclination angles of the shear bands on both sides with the displacement of the trapdoor. The results show that the inclination angle decreases rapidly in the initial and maximum arching stages and slowly decreases in the load recovery stage until reaching the ultimate state. This trend is consistent with the volumetric change rate curve in Fig. 14, indicating that the inclination of the shear band is associated to soil dilatancy effect with shearing due to trapdoor movement.

The development of shear bands, whether deep or shallow condition, is illustrated in Fig. 17. The formation of shear bands or strain localization represents the typical deformation behavior of granular materials, and the dominant factor controlling the development direction of localization (i.e., the inclination angle of the shear band, θ) is the kinematic constraint related to the dilation angle mobilized in the localization region [12]. Dewoolkar et al. [13] and Costa et al. [14]

Table 3

Incremental maximum shear strain γ_{max}^i (%) at different embedment ratios and in typical load evolution stages.

	i = 1	i = 2	i = 3	i = 4
(a) Initial arching ($\delta = 1$ mm; $\Delta = 0.66\%$; point A)				
(b) Maximum arching ($\delta = 2$ mm; $\Delta = 1.33\%$; point B)				
(c) Load recovery ($\delta = 10$ mm; $\Delta = 6.67\%$; point C)				
(d) Ultimate state ($\delta = 20$ mm; $\Delta = 13.33\%$; point D)				

$$0.0 \quad 1.0 \quad 2.0 \quad 3.0 \quad 4.0 \quad 5.0 \quad 6.0 \quad 7.0 \quad 8.0 \quad 9.0 \quad 10.0 \quad \gamma_{max}^i \, (\%)$$

Note: Points A, B, C, and D have been marked in Fig. 3. Incremental maximum shear strain γ_{max}^i (%) represents the change between the current image and previous image with a trapdoor displacement step of 1 mm.

believed that θ was roughly equal to the dilation angle of the soil in their trapdoor test at a specific state. As the amount of plastic volumetric strain is determined by the angle of dilation, further, the direct relation between the plastic strain and inclination of the shear band can be determined. Based on the works of Bolton [36] and Khatami et al. [10], the dilation angle (ψ) at a specific state can be expressed by the strain as Eq. (8) under plane-strain conditions:

$$\psi = \arcsin\left(\frac{C}{R}\right) \tag{8a}$$

$$C = \frac{d\varepsilon_{xx} + d\varepsilon_{yy}}{2} \tag{8b}$$

$$R = \sqrt{\left(\frac{d\varepsilon_{xx} - d\varepsilon_{yy}}{2}\right)^2 + d\varepsilon_{xy}^2} \tag{8c}$$

where C and R are the x-axis component of the center point and radius of the Mohr circle of strain; the letter d represents an incremental response; ε_{xx}, ε_{yy}, and ε_{xy} are the average horizontal strain, vertical strain, and shear strain in a subset zone situated inside the shear band, respectively. Table 3 provides corresponding examples.
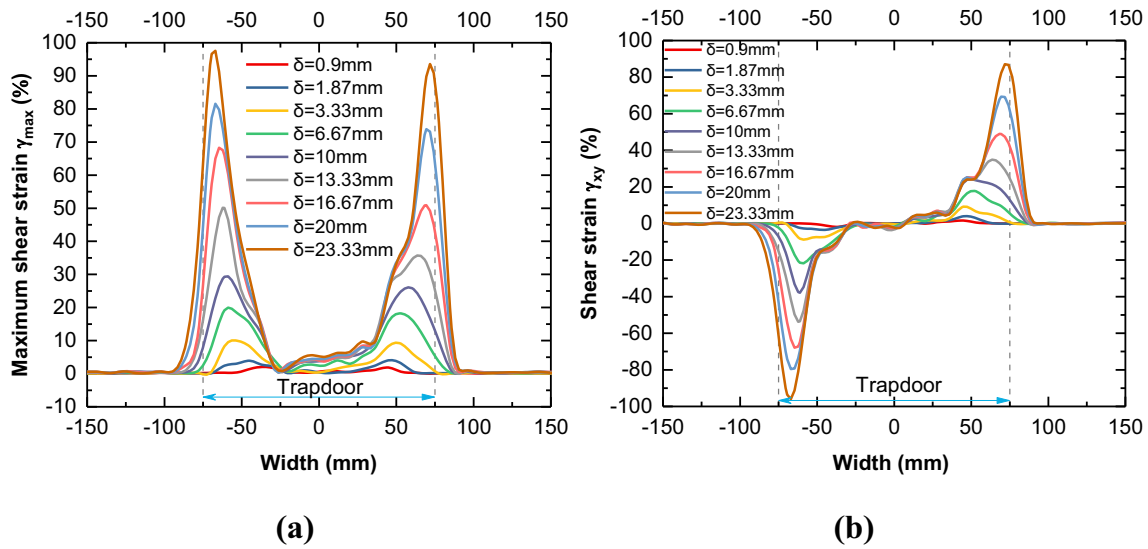
Fig. 15. Distribution and evolution of strain in the horizontal profile at y = 50 mm with the trapdoor displacement (i = 3). (a) Maximum shear strain. (b) Shear strain.
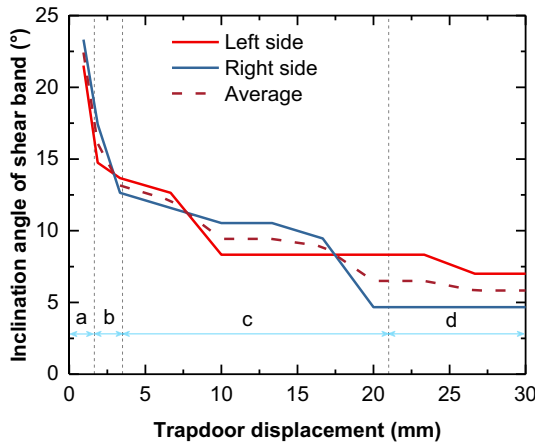

Fig. 16. Development of inclination angles of the shear bands with trapdoor displacement (i = 3).

The interest square subset zones situated inside the shear bands near the edge of the trapdoor were extracted from the strain distributions (Table 3, $i = 3$). θ (initial portion near the edge of trapdoor) and corresponding dilation angle calculated by strain are compared in

Table 4. The calculated dilation angles are close to the measured θ. The shear bands propagate as the inclination angle changes due to mobilization by the dilation effect in soil, as proven by Fig. 14 and Fig. 16. It confirms that θ is equal to ψ, rather than the friction angle φ as mentioned by Iglesia et al. [16] or π/4−φ/2 for the initial shear band as recommended by Rui et al. [28]. Therefore, the critical embedment ratio (i_{cri}) can be deduced as cotψ/2 according to the joining of the shear bands on the surface (shown in Fig. 17). A larger ψ means smaller i_{cri}, for example, for a ψ from 10° to 20°, i_{cri} varies from 2.83 to 1.37. If i<i_{cri}, the shear bands will not intersect with each other. This condition may be the so called the "shear plane arching" termed by Lai et al. [19].

3.3.2. Horizontal and vertical strains

Fig. 18 presents the distributions of the horizontal strain (ε_{xx}). As can be observed, the compressive strain governs the middle strip region. The compressive region is sandwiched by the tensile region. The tensile region approximately coincides with the horizontal displacement region, due to the particles on two sides moving towards the central region. Again, there is no obvious horizontal strain in the parabola region above the trapdoor. Fig. 19 presents the vertical strain (ε_{yy}) at different displacements. An arch strip area across the edge of the trapdoor forms an obvious tensile area. As the trapdoor moves down, the height of this area increases, e.g., from 180 mm to 250 mm. This area is located above the active region because the particle displacement in
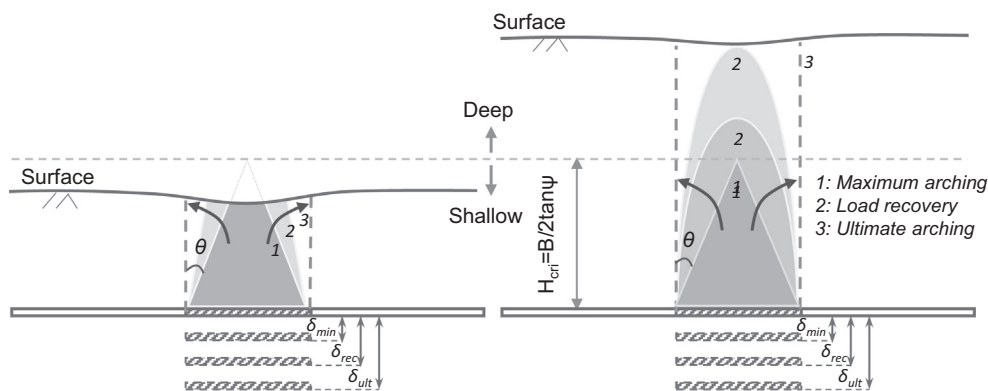

Fig. 17. General illustration of the progressive development of the shear bands in response to the trapdoor receding under shallow and deep conditions.

Table 4
Comparison on the inclination angles of the shear bands and corresponding dilation angles
(i = 3).

Trapdoor displacement δ (mm)	Average inclination angle θ (°)	Dilation angle ψ (°)
1	22.5	21
2	16	11.7
5	12.5	10.1
20	6.5	8.5

$$\Omega = \nabla \times \dot{u} = \begin{vmatrix} e_x & e_y & e_z \\ \dfrac{\partial}{\partial x} & \dfrac{\partial}{\partial y} & \dfrac{\partial}{\partial z} \\ \dot{u}_x & \dot{u}_y & \dot{u}_z \end{vmatrix} \tag{9}$$

where Ω is the vorticity field, $\dot{u}$ is the velocity field, and $\dot{u}_x$, $\dot{u}_y$, and $\dot{u}_z$ are three components of $\dot{u}$, respectively. Here, $\dot{u}_z$ is zero. The mathematical expression of the vorticity is the curl of the velocity field, which physically expresses the flow or relative rotation of the local region. The results show that the distribution of the vorticity field [Fig. 20 (c)] is basically consistent with that of maximum shear strain [Fig. 20 (d)], and obvious local rotation evolution is observed in the shear band region. Therefore, Table 3 also represents the evolution of vorticity. This vorticity is due to the significant velocity gradient and different velocity directions between the active region and the region above it, as shown in Fig. 20 (b). According to the flow characteristics of the granular fill, the velocity field can be simply classified into four distinct regions [Fig. 20 (b)]. (i) Region 1: The parabola region above the trapdoor, i.e., the active region, moves with the trapdoor as a whole, with only vertical movement. (ii) Region 2: The narrow band near the central axis of the trapdoor just above the active region undergoes only vertical movement with a velocity significantly smaller than that of region 1. (iii) Region 3: Two separate regions are present between region 2 and the stationary part, where not only vertical movement, but also obvious horizontal movement can occur. (iv) Region 4: Two separated narrow bands between region 1 and 3 are unique, where the velocity direction changes significantly to transit from region 3 to 1, indicating the relative rotation in local region. Note that these four distinct regions can only be observed when the trapdoor has a relatively large displacement (e.g., in the load recovery stage).

Particularly, the development of velocity with time was calculated. Then, along the elevation of the vertical profile with x = 0 mm [Fig. 20 (a)], the velocity was extracted. As shown in Fig. 21 (a), the velocity of particles $\tilde{v}$ (normalized by trapdoor velocity $v_{trap} = 33.33 \times 10^{-3} mm/s$) declines along the elevation. Anytime, $\tilde{v}$ distribution has a significant gradient at elevations of about 100–300 mm (termed as transition region), which confirms that an invisible arch-shaped structure that spans across the edge of the trapdoor to prevent the flow of particles. In stages a and b, $\tilde{v}$ is obviously smaller than that of the trapdoor (e.g., t = 30, 60, and 100 s). However, in stages c and d, it is almost the same as that of the trapdoor at elevations of 0–100 mm. Moreover, the volume flow rate $\tilde{Q}$ (normalized by volume flow rate above the trapdoor $Q_{trap} = 5 mm^3/s$; unit width) was obtained by velocity field. Fig. 21 (b) presents $\tilde{Q}$ in horizontal section along the elevation, exhibiting similar characteristic as $\tilde{v}$. In stages a and b, both $\tilde{Q}$ and $\tilde{v}$
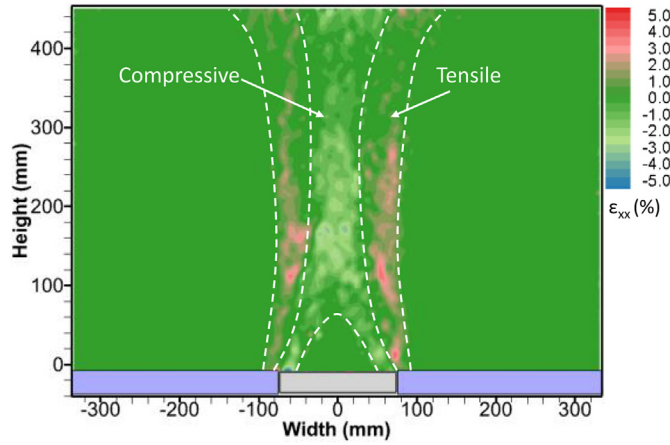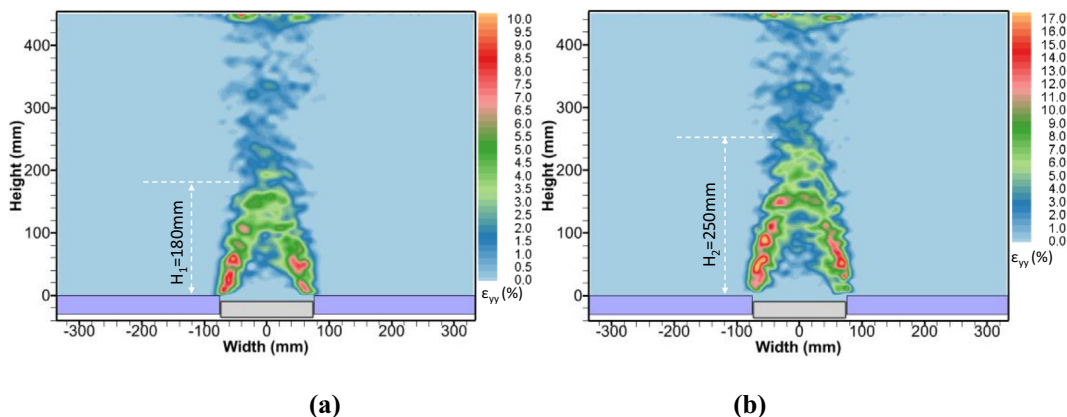

Fig. 18. Distribution of horizontal strains for δ = 10 mm (i = 3).

this area is significantly smaller than that of the trapdoor, creating a tensile area, i.e., a considerably loose zone.

3.4. Particle flow

As the trapdoor moves down, particles are gradually lost, which can be regarded as a particle flow or "sink". Under the gravity-driven flow process, different from silo flow or hopper flow without stress surfaces, supporting effect of trapdoor always exists. The resulting displacement fields [Fig. 20 (a)] were averaged. Then, for an incremental time, the time-average velocity field was deduced as shown in Fig. 20 (b). From the perspective of particle flow, the vorticity of the backfill was calculated by Eq. (9):

(a)

(b)

Fig. 19. Distribution of vertical strains (i = 3). (a) δ = 10 mm. (b) δ = 20 mm.
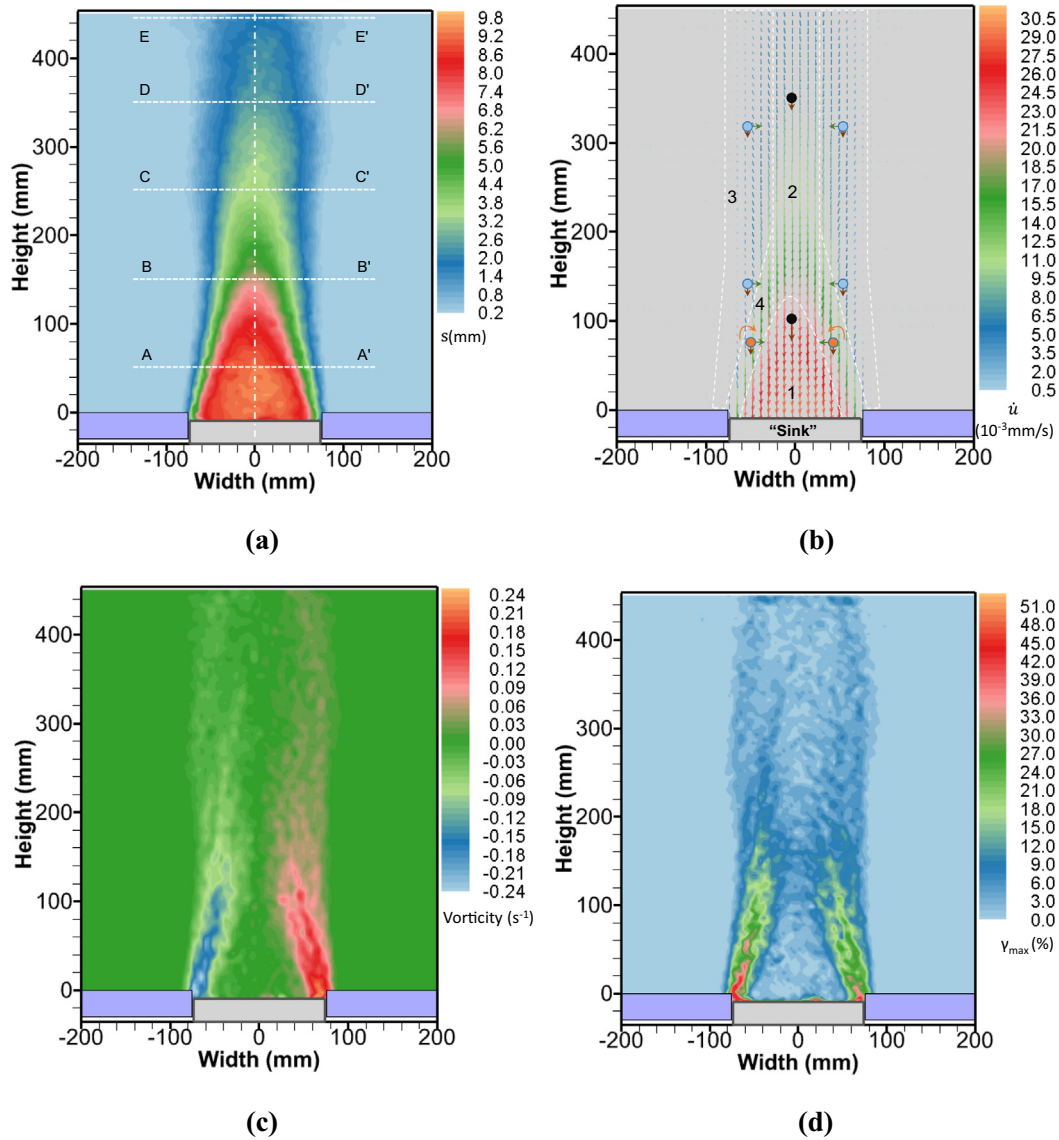
Fig. 20. Computed maximum shear strain, velocity field, and corresponding vorticity field for an image sequence over 300 s ($i = 3$; $\delta = 10$ mm; $t = 300$ s). (a) Displacement. (b) Time-average velocity vector field. (c) Vorticity. (d) Total γ_{max}.

are significantly smaller than that of the trapdoor. It can be speculated that, initially, the static friction force was mobilized between particles. Then, the dislocation and rearrangement between particles results in remarkable volumetric expansion to compensate the volume loss caused by trapdoor. However, in stages c and d, both $\widetilde{Q}$ and $\widetilde{v}$ are approximately equal to that of the trapdoor at elevations of 0–100 mm. It means less jamming occur in the granular flow and the weakening trend of arching effect. Meanwhile, in stages c and d, along the elevation, more remarkable gradients of $\widetilde{Q}$ and $\widetilde{v}$ occur, indicating an increasing porosity of backfill, which will lead to a reduction of shear strength in the granular fill. Consequently, the granular system has experienced a significant structural transition from the initial homogeneous state to the spatially heterogeneous state.

Fig. 22 presents the development of $\widetilde{Q}$ with time at selected horizontal profiles. It is clear that $\widetilde{Q}$ increased rapidly in stages a and b. Then, it increases slowly in stage c, which is consistent with the gradual weakening of arching effect in this stage. In stage d, a steady flow is formed below or near section B-B′ (H = 150 mm), which means that the stable and ultimate arching effect state is reached. In sections C-C′ (H =

250 mm) and D-D′ (H = 350 mm), $\widetilde{Q}$ always keeps an increasing trend. However, some fluctuation characteristics of $\widetilde{Q}$ can be captured, which is closely related to the roof collapse and reformation of arches.

4. Discussion: evolution mechanism of arching

The trapdoor test results show that the load evolution is closely related to the kinematic characteristics of backfill granular materials. Once the trapdoor downwards, a sharp load drop was observed until the maximum arching effect stage, where the magnitude of particle movement is relatively small. Subsequently, conspicuous evolution of the displacement can be observed. A gradual increase in load can occur with the trapdoor displacement until the load becomes constant in the ultimate stage. The evolution mechanisms of arching in these distinct stages should be different. In this section, based on the results of four perspectives, the evolution mechanism will be speculated. Further, the critical displacement between load drop and recovery will be discussed.
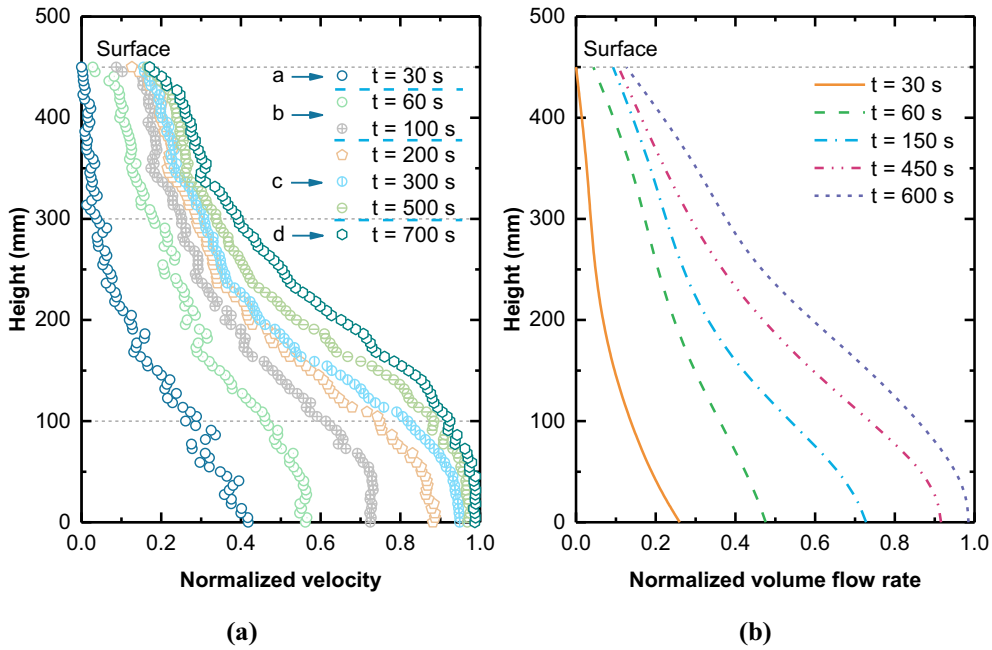
Fig. 21. Velocity and volume flow rate distribution (i = 3). (a) $\tilde{v}$ along the elevation of a vertical profile with $x = 0$. (b) $\tilde{Q}$ in horizontal section along the elevation.
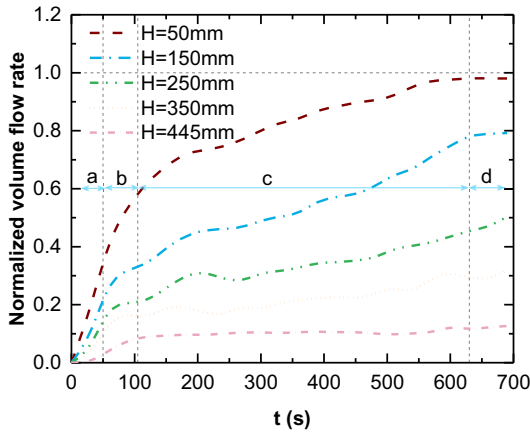

Fig. 22. Variation of $\tilde{Q}$ with time in different horizontal profiles. Sections in Fig. 20 (a): A-A' (H = 50 mm); B-B′ (H = 150 mm); C-C′ (H = 250 mm); D-D′ (H = 350 mm); E-E' (H = 445 mm).

4.1. Load drop mechanism

Mobilization of the maximum shear stress to achieve maximum arching: As shown in Fig. 23 (a), in the initial stage, the downward movement of the trapdoor causes the particles in the overlying triangular region to move down vertically (recall Table 2). Within the boundary of the triangular region, significant mutual extrusion and dislocation with the surrounding static particles will occur, resulting in the development of initial triangular-shaped shear bands with a vertical inclination angle of approximately the maximum dilatancy angle (recall Table 3). The shear stress (τ_s) is quickly mobilized in these shear bands, leading to obvious volumetric expansion of the granular materials in the triangular region to compensate for the volume loss caused by the trapdoor settlement (recall Fig. 13). Therefore, displacement can hardly be observed above the triangular region. Meanwhile, the vertical stress is rapidly transferred (recall Fig. 3) to the trapdoor edges on both sides due to the gradual exertion of the shear stress in the soil body and the reorientation of major principal stress. When the soil arching effects reach the peak state, the maximum value of the shear stress (i.e., peak strength) is mobilized [9]. In this process, the displacement of the soil (s_1) is smaller
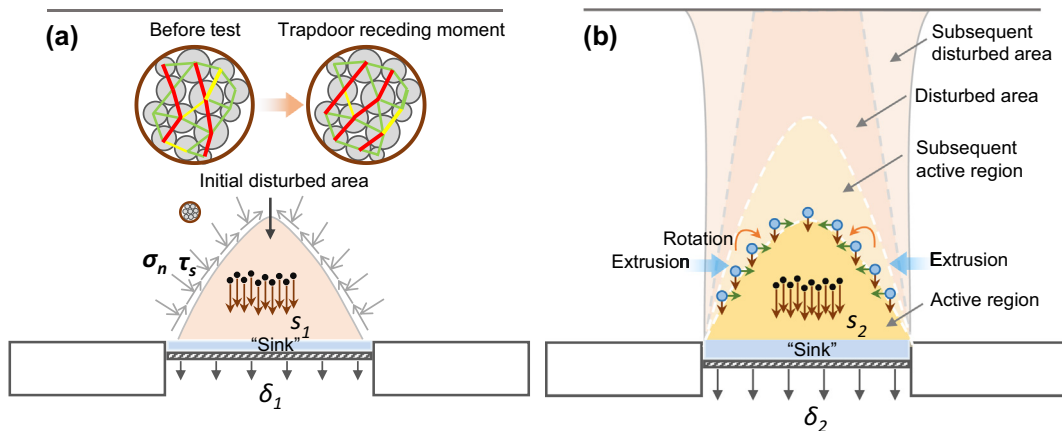

Fig. 23. General illustration of the evolution mechanism of soil arching in distinct stages from macro-and microscopic perspectives. (a) Initial and maximum arching stages (red: main force chain; yellow and green: minor force chain). (b) Load recovery stage.

than trapdoor displacement (δ_1), which may be due to the interlock among granular particles [37]. Regarding the displacement evolution, this process has generally been ignored in previous research as the displacements of the trapdoor and soil are relatively small and difficult to capture. From a microscopic perspective, most of main force chains (FCs) presented a vertical distribution pattern before the trapdoor recedes. At the moment of trapdoor receding, the direction of the main FCs (red) outside the triangle region rotate towards the center, forming a strong "arched force chain bridge" crossing the triangular region and altering the load-transfer path [18,30]. At this stage, mainly the static friction force between particles are mobilized. Due to the initial dense state above triangular region, the strong force chain network at this stage is stable.

4.2. Load recovery mechanism

Evolution of the active region causes the load recovery: As shown in Fig. 23 (b), the initial triangular disturbed region rapidly expands towards the surface, forming a larger region. Meanwhile, the original triangular region evolves into a parabolic region and moves vertically downwards with the trapdoor, i.e., the active region. The overall downward movement of the active region causes the particles in the upper disturbed region to flow towards the region to compensate for the volume loss, as the volumetric expansion in active region is not enough to offset volume loss. These particles move vertically and squeeze the active area horizontally, accompanied by local rotation. From a microscopic perspective, the adjustment of the particle position and posture above the active region causes force chain network change and contact force rotation (Fig. 24); reciprocally, the change of contact force further affects the movement of the particles [38,39]. This interaction process forms an new "arched force chain bridge" as shown in previous DEM studies by Lai et al. [30], preventing the particles from flowing into the active region. Meanwhile, the invisible supporting arch bridge bears part of the load and transfers the vertical load to both sides of the trapdoor. However, as the trapdoor moves further downwards, the force chain bridge buckling as well as the "roof collapse" phenomenon (observed in DEM simulations by Rui et al. [18] and Lai et al. [19]) lead to more particles entering the active region, making the active region evolve upward to form a subsequent active region and achieve a new equilibrium state. This "failure and re-formation" also depends on the trapdoor displacement. In this stage, the force chain network is unstable
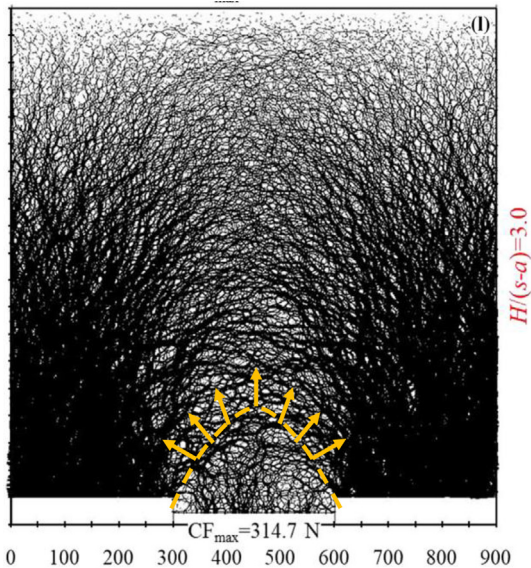
as co-evolution of vortices and FCs [40]. Indirectly, this evolution can be verified from the oscillation characteristic of load recovery curve (recall Fig. 3) and volume flow rate curve (recall Fig. 22), which refers to the instability and fluctuation of these curves. This characteristic has also been observed in previous tests [9,16]. From the perspective of continuum mechanics, an area with a significant displacement gradient is formed above the active region (recall Fig. 21), where a parabola-shaped
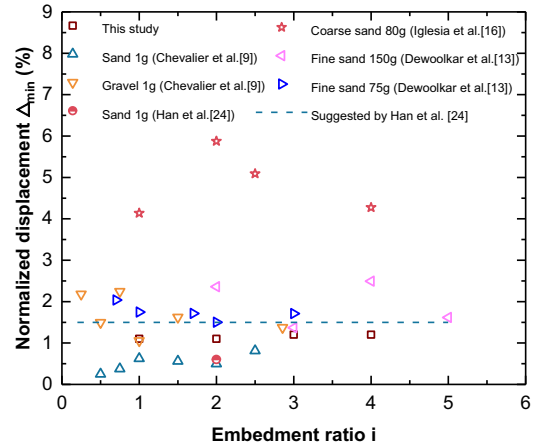
(a)
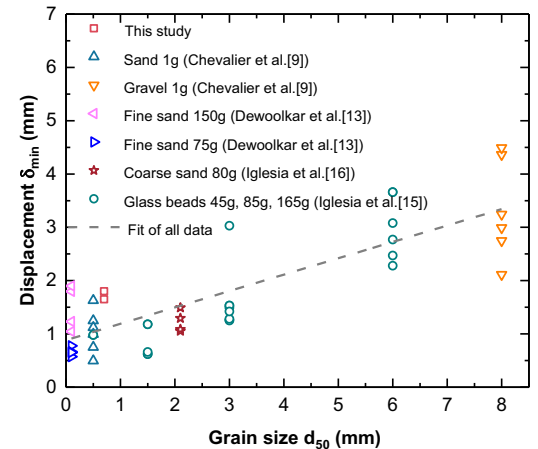
(b)
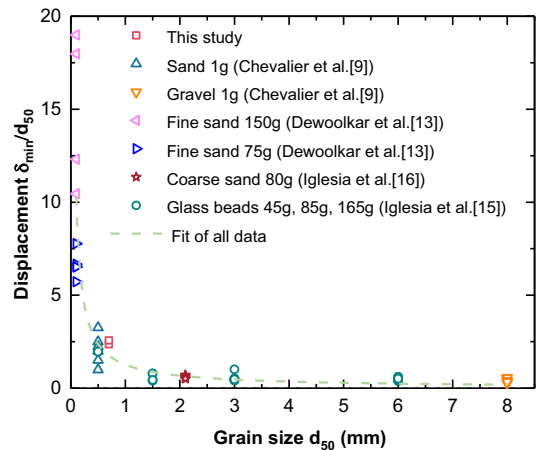
(c)

Fig. 25. Mobilized displacement for maximum arching. (a) Comparison on Δ_{min} with different granular materials and test conditions. (b) δ_{min} versus d_{50}. (c) δ_{min}/d_{50} versus d_{50}.

Fig. 24. Contact force chain bridge to block and support the overlying particles over the active region (contact force chain from Lai et al. [30]; i = 3, δ = 30 mm).

shear band as well as an arch-shaped vertical strain can appear (recall Table 3 and Fig. 19). The upward extension of the active region also leads to a greater load being borne by the trapdoor. Additionally, the residual shear stress (i.e., residual strength) is mobilized for a relatively loose condition above the active region (recall Fig. 19).

4.3. When is the "maximum arching" mobilized?

The normalized displacement Δ_{min} (i.e., the threshold between steady and unsteady state) for mobilizing the minimum load separates the two distinct stages of soil arching evolution, corresponding to the load drop sharply and load recovery stages, respectively. Meanwhile, Δ_{min} is roughly equal to the critical displacement Δ_{cri} for achieving tiny surface settlement. Therefore, accurately assessing the Δ_{min} is conducive to evaluating the evolution stage of the arching effect (e.g., obtaining the vertical load state of the underground structure) and achieving small deformation in practical engineering.

The test results show that a comparatively small displacement is sufficient to achieve the minimum load on the trapdoor or inclusions. Fig. 25 presents the results of this study and previous trapdoor tests, including laboratory 1 g tests [9,24] and centrifuge tests [13,15,16]. The available data show that the minimum load occurs at a trapdoor displacement of about 0.2%–6%, and mainly between 0.5% to 2%, as shown in Fig. 25 (a). Comparing the data for sand and gravel at 1 g, fine sand at 75 g and 150 g, and coarse sand at 80 g demonstrates that Δ_{min} is closely related to the particle characteristics but is not sensitive to the stress level or embedment ratio. The test of coarse sand at 80 g performed by Iglesia et al. [16] shows a relatively larger value of Δ_{min} than the other tests, which may be due to the value of B/d_{50} (24) being smaller than those in the other tests ($B/d_{50} > 200$ except for gravel at 1 g). Han et al. [24] suggested that Δ_{min} can be determined to be 1.5% for a rigid trapdoor. This value may be reasonable when B/d_{50} is large (e.g., $B/d_{50} > 50$) as scale effect can be significantly for small B/d_{50} [15]. Regardless of the embedment ratio and stress level, the data redrawn in Fig. 25 (b) show that the mobilized displacement (δ_{min}: mm) approximately increases with the grain size, indicating that the relative displacement required to mobilize the friction or shear stress fully on failure interface increases with increasing grain size. However, when δ_{min} normalized by d_{50}, δ_{min}/d_{50} decreases significantly with increasing grain size as shown in Fig. 25 (c). Further, more tests and numerical simulation with different granular materials and test conditions should be performed to facilitate estimating a prediction method of Δ_{min} or δ_{min} considering particle characteristics (e.g., grain size and shape) and inclusion width in the future.

5. Conclusions

The evolution characteristics of the arching effect with displacement were comprehensively investigated from four different perspectives. PIV system was developed to obtain important insights into the displacement pattern evolution, shear band propagation, and particle flow characteristics. Further, the mobilization mechanism of the soil arching effect in different load evolution stages was elaborately assessed. The main conclusions can be summarized as follows:

(a) Trapdoor displacement has a significant effect on the load transfer amplitude. The GRC curve, which represented the load response of the soil arching with the relative displacement, could be divided into four distinct stages, namely, the initial arching stage, maximum arching stage, load recovery stage, and ultimate stage. The mobilized displacement (Δ_{min}) for "maximum arching" was closely related to the particle characteristics (e.g., grain size) but was not sensitive to the stress level or embedment ratio. As Δ_{min} has a great significance to determine the evolution stage of the arching effect and achieve a tiny surface settlement, a prediction method of Δ_{min} should be conducted.

(b) The embedment ratio has a significant influence on the evolution of the displacement patterns. The captured disturbed region will experience evolution from the local region with a roughly triangular patterns above the trapdoor to the surface only for deep condition. The maximum value of horizontal displacement occurs in shallow layers near the surface for the shallow condition, whereas it appears in deep layers for the deep condition.

(c) The dilatancy behavior has a significant effect on the deformation mechanism and development of shear bands. An obvious shear dilatancy behavior and density change accompanied the trapdoor moving downwards, especially in the initial and maximum arching stages. The progressive formation of shear bands could be better explained by considering the dilatancy behavior and strain localization. The local inclination of the shear band could be predicted by the dilation angle calculated by incremental shear strain. According to the joining of the primary shear bands on the surface, the critical embedment ratio (i_{cri}) can be identified as $\cot\psi/2$.

(d) The vorticity field distribution was basically consistent with that of maximum shear strain, and obvious local rotation evolution was observed in the shear band region. Four distinct regions could be identified according to the flow characteristics, which provide an opportunity for understanding the evolution mechanism of soil arching. Importantly, an active region with a parabolic shape that existed above the trapdoor drop vertically as an entire block. An invisible supporting structure formed above the active region to jam the particle flow.

(e) The evolution mechanism of soil arching was different in distinct stages. In the initial and maximum arching stage, a triangular region was observed with obvious volumetric expansion to compensate for the volume loss and support the upper stationary part. The maximum shear stress was mobilized with small displacement to achieve maximum arching. Differently, the evolution of the disturbed region caused load recovery in the subsequent stage.

Due to the inherent complexity of trapdoor arching, there is currently no established, universal mechanism or mobilized shape to describe the evolution of arching, especially as the failure pattern changes with increasing settlement of trapdoor. The physical reasons for this observation include geometric, environmental and geotechnical factors such as buried depth, soil dilation, grain packing density [37,41,42], stress level [13], moisture content [43], particle characteristics [31,33,44], stress history, and surcharge [8,14,28], which can be considered in the future. Despite the limitations, this study provides comprehensive perspectives regarding the evolution of the arching effect. In particular, it links the load evolution mechanism with the deformation behavior of backfill, providing an enhanced basis for displacement-related mathematical modelling of arching in the future.

Credit author statement

Yu Zhao: Methodology, Laboratory investigation, Analysis and interpretation of data, Writing - original draft. **Quan-mei Gong**: Conceptualization, Supervision, Funding acquisition. **Yao-jie Wu**: Laboratory investigation, Writing - review & editing. **Jorge G. Zornberg**: Writing - review & editing. **Zhi-yao Tian:** Analysis and interpretation of data, Visualization. **Xiao Zhang**: Analysis and interpretation of data.

Declaration of Competing Interest

The authors declare that they have no known competing financial interests or personal relationships that could have appeared to influence the work reported in this paper.

Acknowledgements

References

[1] K. Terzaghi, Theoretical Soil Mechanics, John Wiley and Sons Inc 1943.

[2] A. Marston, A.O. Anderson, The Theory of Loads on Pipes in Ditches and Tests of Cement and Clay Drain Tile and Sewer Pipe, Iowa State College of Agriculture and Mechanic Arts, Ames, Iowa, 1913.

[3] C.H. Evans, An Examination of Arching in Granular Soils. SM. Thesis Cambridge, MA, Dept. of Civil Engineering, MIT, 1983.

[4] T. Tanaka, T. Sakai, Progressive failure and scale effect of trap-door problems with granular materials, Soils Found. 33 (1) (1993) 11–29.

[5] G.R. Iglesia, H.H. Einstein, R.V. Whitman, Determination of vertical loading on underground structures based on an arching evolution concept, in: G. Fernandez, R.A. Bauer (Eds.), Proceedings of the Third National Conference on Geo-Engineering for Underground Facilities, ASCE, Reston, VA 1999, pp. 495–506.

[6] H. Khatami, A. Deng, M. Jaksa, An experimental study of the active arching effect in soil using the digital image correlation technique, Comput. Geotech. 108 (2019) 183–196.

[7] Q.Y. Yao, H.G. Di, C. Ji, S.H. Zhou, Ground collapse caused by shield tunneling in sandy cobble stratum and its control measures, B Eng Geol Environ 2 (2020) 1–16.

[8] I. Vardoulakis, B. Graf, G. Gudehus, Trap-door problem with dry sand: a statical approach based upon model kinematics, Int J Anal Meth Geomech 5 (1981) 57–78.

[9] B. Chevalier, G. Combe, P. Villard, Experimental and discrete element modeling studies of the trapdoor problem: influence of the macro-mechanical frictional parameters, Acta Geotech. 7 (1) (2012) 15–39.

[10] H. Khatami, A. Deng, M. Jaksa, Passive arching in rubberised sand backfills, Can. Geotech. J. 57 (2019).

[11] Y.D. Costa, J.G. Zornberg, Active and passive arching stresses outside a deep trapdoor, Acta Geotech, 2020 https://doi.org/10.1007/s11440-020-00969-x.

[12] J.K. Stone, Modelling of rupture development in soils PhD. dissertation, Wolfson College, Cambridge Univ, 1988.

[13] M.M. Dewoolkar, K. Santichaianant, H.-Y. Ko, Centrifuge modeling of granular soil response over active circular trapdoors, Soils Found. 47 (5) (2007) 931–945.

[14] Y.D. Costa, J.G. Zornberg, B.S. Bueno, C.L. Costa, Failure mechanisms in sand over a deep active trapdoor, J. Geotech. Geoenviron. Eng. 135 (11) (2009) 1741–1753.

[15] G.R. Iglesia, H.H. Einstein, R.V. Whitman, Validation of centrifuge model scaling for soil systems via trapdoor tests, ASCE J Geotech Geoenviron Eng 137 (11) (2011) 1075–1089.

[16] G.R. Iglesia, H.H. Einstein, R.V. Whitman, Investigation of soil arching with centrifuge tests, ASCE J Geotech Geoenviron Eng 140 (2) (2014), 04013005, .

[17] G.S. Pardo, E. Saez, Experimental and numerical study of arching soil effect in coarse sand, Comput Geotech 57 (apr.) (2014) 75–84.

[18] R. Rui, A.F. van Tol, X.L. Xia, S.J.M. van Eekelen, G. Hu, Y.Y. Xia, Evolution of soil arching; 2D DEM simulations, Comput. Geotech. 73 (2016) 199–209.

[19] H.J. Lai, J.J. Zheng, R.J. Zhang, M.J. Cui, Classification and characteristics of soil arching structures in pile-supported embankments, Comput. Geotech. 98 (2018) 153–171.

[20] C.C. Qi, A. Fourie, Numerical investigation of the stress distribution in backfilled stopes considering creep behaviour of rock mass, Rock Mech. Rock. Eng. 52 (2019) 3353–3371.

[21] W.J. Hewlett, M.F. Randolph, Analysis of piled embankment, Ground Eng. 21 (3) (1988) 12–18.

[22] S.J. Feng, S.G. Ai, H.X. Chen, H.J. Xie, An analytical method for predicting load acting on geosynthetic overlying voids, Geotext. Geomembr. 45 (6) (2017) 570–579.

[23] X. Zhao, A. Fourie, C.C. Qi, An analytical solution for evaluating the safety of an exposed face in a paste backfill stope incorporating the arching phenomenon, Int. J. Miner. Metall. Mater. 26 (10) (2019) 1206–1216.

[24] J. Han, F. Wang, M. Al-Naddaf, C. Xu, Progressive development of two-dimensional soil arching with displacement, Int J Geomech 17 (12) (2017), 04017112, .

[25] E. Papamichos, I. Vardoulakis, L.K. Heil, Overburden modeling above a compacting reservoir using a trap door apparatus, Phys. Chem. Earth A 26 (1–2) (2001) 69–74.

[26] D.J. King, A. Bouazza, J.R. Gniel, R.K. Rowe, H.H. Bui, Serviceability design for geosynthetic reinforced column supported embankments, Geotext. Geomembr. 45 (4) (2017) 261–279.

[27] S.H. Zhou, B.L. Wang, Y. Shan, Review of research on high-speed railway subgrade settlement in soft soil area, Rail Eng Science 28 (2) (2020) 129–145.

[28] R. Rui, A.F. van Tol, Y.-Y. Xia, S.J.M. van Eekelen, G. Hu, Investigation of soil-arching development in dense sand by 2D model tests, Geotech. Test. J. 39 (3) (2016) 415–430.

[29] S. Jacobsz, Trapdoor experiments studying cavity propagation, in: S. Jacobsz (Ed.), Proceedings of the First Southern African Geotechnical Conference, CRC Press 2016, pp. 159–165.

[30] H.J. Lai, J.J. Zheng, M.J. Cui, J. Chu, "soil arching" for piled embankments: insights from stress redistribution behaviour of dem modelling, Acta Geotech. 15 (8) (2020) 2117–2136.

[31] H. Khatami, A. Deng, M. Jaksa, The arching effect in rubber–sand mixtures, Geosynth Int. 4 (27) (2020).

[32] Q.M. Gong, Y. Zhao, J.H. Zhou, S.H. Zhou, Uplift resistance and progressive failure mechanisms of metro shield tunnel in soft clay, Tunn Undergr Sp Tech 82 (2018) 222–234.

[33] Z.Q. Bi, Q.M. Gong, P.J. Guo, et al., Experimental study of the evolution of soil arching effect under cyclic loading based on trapdoor test and particle image velocimetry, Can. Geotech. J. 57 (2020).

[34] D.J. White, W.A. Take, M.D. Bolton, Soil deformation measurement using particle image velocimetry (PIV) and photogrammetry, Geotechnique 53 (7) (2003) 619–631.

[35] X. Peng, J.G. Zornberg, Evaluation of soil-geogrid interaction using transparent soil with laser illumination, Geosynth. Int. 26 (2) (2019) 206–221.

[36] M.D. Bolton, The strength and dilatancy of sands, Géotechnique 36 (1) (1986) 65–78.

[37] M.I. Peerun, D.E.L. Ong, C.S. Choo, W.C. Cheng, Effect of interparticle behavior on the development of soil arching in soil-structure interaction, Tunn Undergr Sp Tech 106 (2020).

[38] S.H. Zhou, P.J. Guo, D.F.E. Stolle, Interaction model for "shelled particles" and small-strain modulus of granular materials, J App Mech 85 (10) (2018) 101001.

[39] J.H. Xiao, S. Sun, X. Zhang, D. Zhang, K. Wei, Y. Wang, Macro and meso dynamic response of granular materials in ballastless track subgrade for high-speed railway, Int J Transport Sci Tech (2020) https://doi.org/10.1016/j.ijtst.2020.09.001.

[40] A. Tordesillas, S. Pucilowski, Q. Lin, J.F. Peters, R.P. Behringer, Granular vortices: identification, characterization and conditions for the localization of deformation, J Mech Phys Solids 90 (may) (2016) 215–241.

[41] T. Eskisar, J. Otani, J. Hironaka, Visualization of soil arching on reinforced embankment with rigid pile foundation using X-ray CT, Geotext. Geomembr. 32 (2012) 44–54.

[42] E. Badakhshan, A. Noorzad, A. Bouazza, Y.F. Dafalias, L. King, Load recovery mechanism of arching within piled embankments using discrete element method and small scale tests, Powder Technol. 359 (2020).

[43] P.J. Guo, S.H. Zhou, Arch in granular materials as a free surface problem, Int J Numer Anal Met 37 (9) (2013) 1048–1065.

[44] R.P. Chen, Q.W. Liu, H.N. Wu, H.L. Wang, F.Y. Meng, Effect of particle shape on the development of 2D soil arching, Comput. Geotech. 125 (2020) 153–171.